Applied Surface Science 580 (2022) 152289

Contents lists available at ScienceDirect

Applied Surface Science

journal homepage: www.elsevier.com/locate/apsusc

Full Length Article

Phase and microstructure control of electrodeposited Manganese Oxide with enhanced optical properties

Roberto Cestaro [a,b,*], Peter Schweizer [a], Laetitia Philippe [a], Xavier Maeder [a], Albert Serrà [a]

[a] Empa Swiss Federal Laboratories for Materials Science and Technology, Laboratory for Mechanics of Materials and Nanostructures, CH-3602 Thun, Switzerland
[b] Ecole Polytechnique Fédérale de Lausanne, Tribology and Interface Chemistry Group, EPFL SCI STI SM, Station 12, CH-1015 Lausanne, Switzerland

ARTICLE INFO

Keywords:
Manganese Oxide
Electrodeposition
Microstructure Control
Phase Composition
Optical Properties

ABSTRACT

Mn_3O_4 and Mn_2O_3 were synthesized by potentiostatic electrodeposition from a de-aerated manganese acetate and sodium sulfate electrolytic bath, followed by annealing. The electrodeposition parameters (including applied potential, precursor concentration, pH, temperature) and the thermal treatment conditions were investigated to obtain the best control over microstructure and stoichiometry of manganese oxides. We found that the applied voltage is the key parameter affecting the valence state of initial amorphous manganese while the thermal treatment leads to crystallization and tuning of optical properties without substantially changing the morphology. The as-electrodeposited manganese oxides are X-rays amorphous, while two different crystalline phases, Mn_3O_4 and Mn_2O_3, were obtained after the thermal treatment depending on the applied voltage. Through the analysis of TEM cross section images, a fiber-like growth was observed for Mn_3O_4, while Mn_2O_3 presented a less porous-more compact microstructure. The optical properties were investigated, resulting in an enhancement in the charge separation properties of the thermally treated manganese oxides, reflected by nearly a 40 % reduction in the photoluminescence peak intensity. We believe that these finding will be useful in the future development of environmental friendly manganese oxide-based photoelectrochemical systems.

1. Introduction

Manganese oxides (MnO_x) poly-types such as MnO, Mn_2O_3, MnO_2, and Mn_3O_4 show non-toxic behavior, environmental compatibility, high specific capacitance and attractive catalytical properties and therefore hold great promise for sustainable nanotechnology [1–3]. Manganese oxides-based materials can be prepared via a variety of techniques, including hydrothermal, chemical bath deposition, sol–gel, electrodeposition, solvothermal, and co-precipitation methods [4–8]. Electrodeposition was proven to be an effective method to prepare MnO_x nanostructures since the process requires low initial capital investment and provides high production rates with few shape and size limitations [9–11].

However the electrodeposition of manganese oxide still presents numerous challenges concerning the control of the final valence state of Mn and the reproducibility of the synthesis process. This is due to the multiple stable oxidation states of manganese (Mn(II), Mn(III), Mn(IV)) that can be obtained by electro-oxidation of Mn^{2+} precursors. The electrodeposition of MnO_2 is based on a well-known mechanism, but the synthesis of other stoichiometric variants like Mn_3O_4 and Mn_2O_3 is less understood [12].

For example Chen *et al.* [13] studied the temperature-dependent phase transition of manganite (MnOOH) nanowires. A 3 h thermal treatment in nitrogen produced tetragonal Mn_3O_4 in the whole temperature range (400 – 1100 °C), while in air atmosphere the phase transformation to tetragonal Mn_3O_4 (400 °C), cubic Mn_2O_3 (600 °C) and tetragonal Mn_3O_4 (1100 °C) were obtained. Similarly, Deljoo and co-workers [14] investigated the thermally activated structural transformations in amorphous manganese oxide nanoparticles under air and argon atmospheres. During heat treatment in air, MnO_2 nanoparticles were reduced to cubic Mn_2O_3 at 500 °C, followed by a transformation to tetragonal Mn_3O_4 at 1010 °C, and to cubic Mn_3O_4 at 1190 °C. The samples heat-treated in argon firstly crystallized to a mixture of monoclinic Mn_2O_3 and tetragonal Mn_3O_4 at 475 °C, followed by complete transformation to tetragonal Mn_3O_4 at 820 °C, and then to mostly cubic MnO at 1145 °C.

Therefore, most of the stable manganese oxides can be obtained from MnO_2 by annealing under appropriate conditions. However, the correlation between the synthesis parameters and the final composition and crystal structure of the electrodeposited manganese oxides is still

* Corresponding author.
E-mail address: roberto.cestaro@empa.ch (R. Cestaro).

https://doi.org/10.1016/j.apsusc.2021.152289
Received 27 September 2021; Received in revised form 8 December 2021; Accepted 18 December 2021
Available online 22 December 2021

partially unknown. Up to now research was mainly focused on varying the electrodeposition parameters to obtain manganese oxides with the best capacitive properties [15–23]. Mathur *et al.* [24] studied the electrochemical and photoelectrochemical energy conversion properties of (α + δ)-MnO_2 composite, revealing a beneficial synergistic effect between the two crystallographic phases, tunnel structure α-MnO_2 and layered δ-MnO_2. Smith and coworkers [25] investigated the catalytic activity for water oxidation of MnOOH, β-, γ-, δ-MnO_2 and Mn_2O_3. Their results showed that corner-sharing Mn^{3+} is more catalytically active compared with edge-sharing Mn^{3+} or Mn^{4+} in any coordination environment. Many other examples of comparison between the (photo)catalytic properties of different MnO_2 polymorphs and stoichiometric variants can be found in literature [26–30]. In this paper we present the synthesized Mn_2O_3 and Mn_3O_4 in a two-step process: (i) electrodeposition from a deaerated Mn^{2+} electrolytic bath; (ii) thermal treatment at 450 °C for 1 h in air atmosphere. The effect of the electrodeposition parameters and the subsequent thermal treatment on the final surface morphology, microstructure, crystallinity, oxidation state and optical properties of the MnO_x nanostructures has been investigated. As a result, this work provides a clear and innovative method to obtain different manganese oxides by tuning the applied potential.

This is of utmost importance considering the control over phase and microstructure as the first requirement towards a further comprehension and characterization of manganese oxides properties.

2. Material and methods

2.1. Synthesis of manganese oxides nanostructures

Manganese oxides nanostructures were synthetized by potentiostatic electrochemical deposition using a standard three-electrode electrochemical cell at room temperature. A deaerated electrolyte composed of manganese acetate, $MnAc_2$ (Sigma Aldrich > 98 %) in variable concentration (0.5 mM – 50 mM) and 100 mM sodium sulphate, Na_2SO_4 (Fluka > 99.0 %) was used. A working electrode of Fluorine-doped Tin Oxide (FTO) covered glass (Sigma Aldrich, ~ 7 Ω/sq) was cleaned with soapy water and ultrasonicated for 10 min in deionized water, acetone and isopropanol prior the electrodeposition. A Pt wire and a Ag/AgCl 3 M KCl were used as counter and reference electrode, respectively. The electrodeposition was performed potentiostatically with an Autolab PGSTAT30 at different step potentials in the range 0.6 V – 1.4 V with a charge density of 50 mC/cm^2. The pH and the temperature of the electrolytic bath were maintained at a fixed value during the synthesis. Deposition experiments were performed in a pH range from 5.5 to 7.5, while the solution temperature was varied between 25 °C, 50 °C and 75 °C. After the electrodeposition, the FTO glass with manganese oxide deposit was immersed in 50 °C distilled water and dried in air at room temperature. Finally, a thermal treatment at 450 °C (5 °C/min) for 1 h in air atmosphere was performed using a rapid thermal annealing equipment (Advanced Riko Mila 5050).

2.2. Characterization of the manganese oxide nanostructures

The morphology of manganese oxide nanostructures was characterized by field-emission scanning electron microscopy (FE-SEM, Hitachi S-4800). X-ray diffraction (XRD, Bruker D8 Discovery diffractometer) in the Bragg–Brentano configuration, Cu K_α radiation, was used to determine the crystal phases. The X-ray photoemission spectroscopy (XPS) measurements were performed using the Al K_α line (1486.6 eV, 350 W) of a PHI 5600 Multitechnique, Physical Electronics. To analyze the morphology, crystallinity and local chemistry of the deposited films, Transmission Electron Microscopy (TEM) was performed using a probe-corrected Thermo Fisher Scientific Titan Themis 200 G3 outfitted with a SuperX detector. All TEM measurements were performed at 200 keV electron energy. HRSTEM image simulations were performed using the Prismatic software (C Ophus, A fast image simulation algorithm for scanning transmission electron microscopy. Advanced Structural and Chemical Imaging 3(1), 13 (2017)). The optical properties were tested by UV–Vis spectroscopy (PerkinElmer Lambda 900 UV spectrophotometer). Photoluminescence (PL) emission spectra were obtained using a Hitachi F7000 fluorescence spectrophotometer with excitation at 315 nm.

3. Results and discussion

3.1. Cyclic voltammetry

Despite the availability of several Mn(II) precursors, we chose to use manganese acetate since it has the higher deposition rate at lower potentials with respect to the other precursors [31]. The CVs recorded in presence and absence of manganese acetate are reported in Fig. 1 (red and black line, respectively).

The CV recorded in absence of $MnAc_2$ (black line) does not show any peak in the selected range of potential, confirming the inertia of the supporting electrolyte and the substrate in the electrochemical process. When manganese acetate is added in the electrolytic bath, the recorded CV displays two oxidation and two reduction peaks. The researchers agreed to attribute the two cathodic peaks to the reduction of Mn(IV) based on the early work of Rodrigues *et al.* [32]. To further support this assertion, the inset in Fig. 1 shows that the two cathodic peaks are still present when the CV is recorded to a lower applied potential, avoiding O_2 evolution. In the anodic part of the voltammogram the O_2 evolution due to the water oxidation is represented by the peak at 1.4 V, while the peak centered at 0.8 V is assigned to the oxidation of Mn(II) to Mn(IV). The majority of the literature distinguishes two different electrodeposition pathways based on the pH of the electrolytic bath for the electrooxidation of Mn^{2+}: an ECE (two electrochemical steps separated by a chemical step) or a disproportionation (a single electrochemical step followed by two chemical steps) process. The first common step is the oxidation of Mn^{2+} to Mn^{3+}. At high pH values the metastable Mn^{3+} ions undergo hydrolyzation to form MnOOH which is then oxidized to MnO_2 (ECE mechanism). In highly acidic conditions, Mn^{3+} ions are more stable and can disproportionate to form Mn^{2+} and MnO_2 (disproportionation mechanism). Even though it should be expected to observe two oxidation peaks for the ECE and a single oxidation peak for the disproportionation process, however the cyclic voltammetry is unable to distinguish between the two of them since both traces show only one

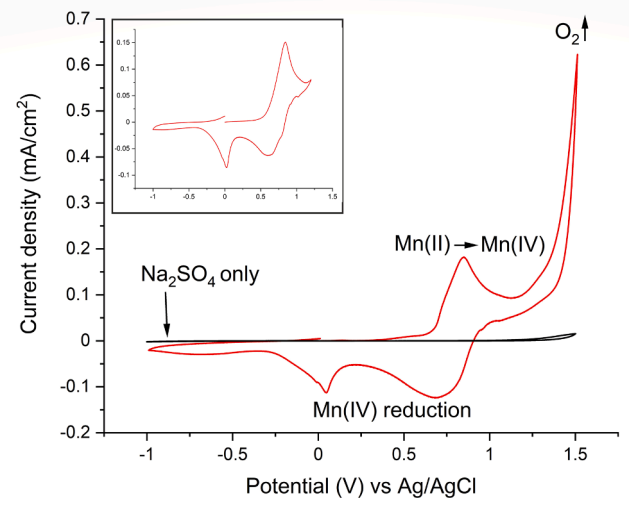

Fig. 1. Cyclic voltammograms. Solution 0.5 mM $MnAc_2$ and 100 mM Na_2SO_4 (red line) measured with a scan rate of 50 mV/s at pH 7.5 and room temperature. The black line represents the CV in absence of $MnAc_2$ measured in the same bath pH and temperature conditions. Inset: CV recorded to a lower applied potential.

single oxidation peak [10,11,16,20,32–34]. Besides, presence of dissolved O_2 in the electrolyte does not significantly affect the voltammogramm [16].

3.2. Effect of the electrodeposition parameters on the surface morphology of as-deposited MnOx

The supersaturation ratio at the electrode/electrolyte interface is the main factor that enables to predict and control the kinetics of nucleation and growth during the electrodeposition. Considering the expected reaction for the anodic electrodeposition of MnO_2 (Eq. (1)):

$$Mn^{2+}{}_{(aq)} + 4OH^- \rightarrow MnO_{2(s)} + 2H_2O + 2e^- \quad (1)$$

The supersaturation ratio (S) is defined in Eq. (2) as:

$$S = \frac{(\alpha_{Mn^{2+}})(\alpha_{OH^-})^4}{(\alpha_{Mn^{2+}{}_e})(\alpha_{OH^-{}_e})^4} \quad (2)$$

where α is the activity of the ions in the electrolytic bath at actual or equilibrium condition.

The supersaturation ratio can be tuned by changing the electrodeposition parameters such as solution concentration, pH and temperature, as well as by applying a higher or lower step potential. To verify the influence of those parameters, we performed a systematic study by varying only one parameter at time while all the other parameters remain unchanged. The fixed parameters were: 1.0 V applied voltage, solution 50 mM $MnAc_2$ at pH 7.5 and room temperature. The results are reported in the Supporting Information, Figures S1 – S5. In this document is only reported in Fig. 2 a summary of the different MnO_x surface morphologies obtained through the control of the electrodeposition parameters.

It is well known that the supersaturation is proportional to the deposition rate, therefore higher values of S are correlated to a faster deposition process [21,22].

At low deposition rate the progressive nucleation is the main ongoing process: in this condition, fewer and larger nuclei are formed resulting in the development of a rough surface composed of the discrete manganese oxide clusters.

With the increase of the supersaturation, the deposition rate is accelerated, and many MnO_x nuclei are deposited forming a more continuous morphology consisting of interconnected thin sheets forming coarser petal-shaped flakes. The nanoflakes are refined as the deposition rate further increases, according to the faster nucleation rate with respect to the nuclei growth.

The purpose of this first investigation was to understand the relationship between the electrodeposition parameters and the final surface morphology of manganese oxides. Considering that a high specific surface area is beneficial for the catalytic properties of MnO_x, we established the optimized working conditions as following: applied voltage 0.6 V and 1.0 V, 50 mM $MnAc_2$, pH 7.5, 25 °C.

3.3. Surface morphology and microstructure control of annealed MnOx

In Fig. 3 SEM images of the 0.6 V (a) and 1.0 V (b) manganese oxides as well as cross sectional STEM images are reported.

The comparison between the different surface morphologies as a function of the applied voltage has been already reported in Figure S4 of the Supporting Information. Interconnected nanosheets with petal-like morphology or nanoflakes are developed when the applied voltage is 0.6 V or 1.0 V respectively. According to the thermodynamics of the electrodeposition reaction, the deposition rate is faster when a higher potential is applied (Eq. (2)). This allows an easier charge transfer and therefore the formation of a finer surface morphology. To have a complete overview of the MnO_x microstructure, STEM cross section images of the electrodeposited manganese oxides are reported in Fig. 3c and 3d. A fibrous growth with an open porosity is present when 0.6 V are applied, while a higher applied voltage results in a more compact microstructure with a smaller porosity. As a consequence, the deposited film is thicker for the 0.6 V sample despite the amount of deposited charges was fixed at 50 mC/cm^2 during the electrodeposition step for both the samples. EDX colors maps reported in Fig. 3e – 3 h confirm the presence of Mn and O uniformly distributed along the thickness of the deposit for both the samples.

All the aforementioned considerations emphasize the huge effect of the applied potential on the surface morphology and microstructure of the final MnO_x. Luckily, the electrodeposition technique allows a very precise control of the applied potential, therefore enabling the production of manganese oxides with different properties, as demonstrated in the Section 3.5.

3.4. Phase control of annealed MnOx

The electrodeposition parameters can affect not only the surface morphology but also the crystallinity and the oxidation state of the manganese oxide nanostructures. Fig. 4 reproduces the X-ray diffractograms of the FTO-glass substrate and the MnO_x nanostructures before and after the thermal treatment.

As shown in Fig. 4c, the X-ray diffractograms of all the as-electrodeposited MnO_x nanostructures is X-rays amorphous independently on the synthesis parameters. Therefore, the effect of the electrodeposition parameters is only limited to favor/prevent the mass diffusion of Mn(II) ions at the electrode, affecting the morphology of the manganese oxide structures (see Supporting Information Figures S1 – S5). This is in accordance with the previously reported studies [35–37]. Depending on the applied potential during the electrodeposition process, the thermally treated manganese oxides develop two different crystalline structure, tetragonal Mn_3O_4 and cubic Mn_2O_3 for the samples synthetized in the range 0.6 V – 0.8 V and 1.0 V – 1.4 V respectively. Based on these results we performed a TEM cross-section analysis on the manganese oxides synthetized by applying 0.6 V and 1.0 V and subsequently annealed. Fig. 5a and 5d represent overview bright-field TEM

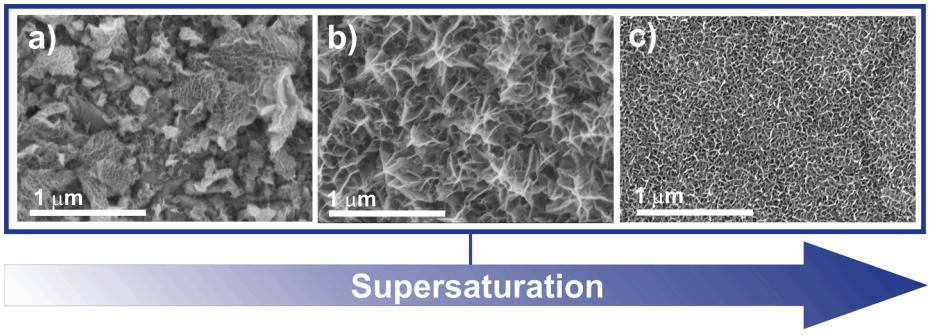

Fig. 2. Morphology of the MnO_x structures at different supersaturation. a) Low deposition rate [pH 7.5, 1.0 V, 0.5 mM $MnAc_2$, 25 °C], b) medium deposition rate [pH 7.5, 0.6 V, 50 mM $MnAc_2$, 25 °C], c) high deposition rate [pH 7.5, 1.4 V, 50 mM $MnAc_2$, 25 °C]. Scale bar: 1 µm.

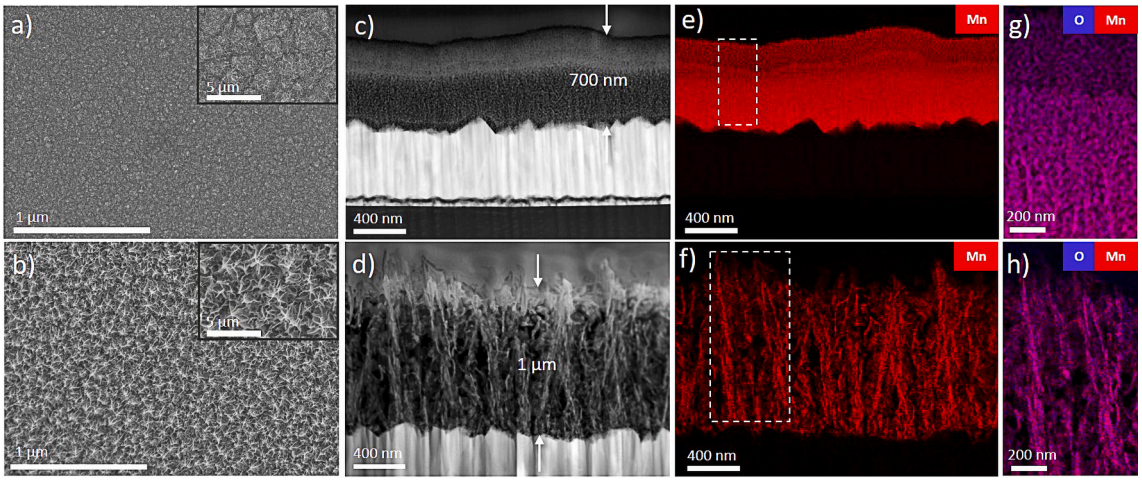

Fig. 3. Morphological and compositional analysis. SEM top-view images of the 1.0 V (a) and 0.6 V (b) samples. c) & d) STEM images of the cross section of both samples showing the difference in layer thickness and density. EDX maps (e-h) show the homogenous distribution of Mn and O throughout the film.

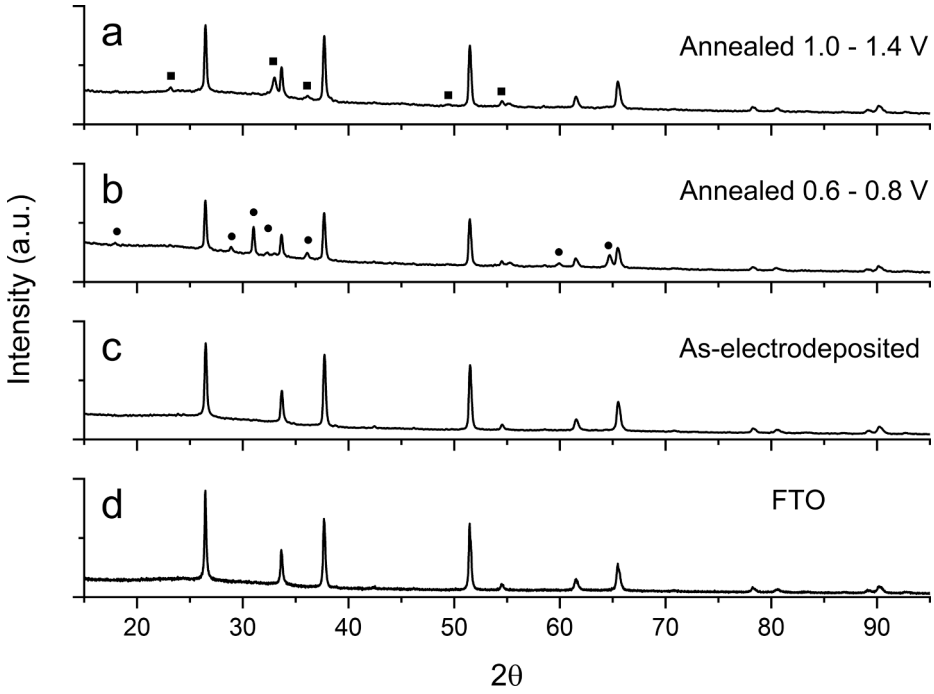

Fig. 4. X-ray diffractograms. a) Annealed MnO_x nanostructures obtained by applying 1.0 V – 1.4 V; b) annealed MnO_x nanostructures obtained by applying 0.6 V – 0.8 V; c) as-electrodeposited MnO_x; d) FTO-glass substrate. Reference X-ray diffractograms are illustrated for Mn_2O_3 (black square) and for Mn_3O_4 (black circle).

images of both samples, showing the difference in layer thickness and morphology.

The insets in Fig. 5b and 5e show representative selected-area electron diffraction (SAED) patterns obtained from the 0.6 V and 1.0 V annealed MnO_x. In both cases the diffraction patterns display multiple Bragg reflections, suggesting a polycrystalline nature of the samples. The radially integrated intensity profiles (Fig. 5b and 5e) are consistent with a mixture of Mn_3O_4 and Mn_2O_3 for the 0.6 V sample and pure Mn_2O_3 phase for the 1.0 V. Those results are in good agreement with the XRD even though the Mn_2O_3 phase in the 0.6 V sample was not detected. This could be due to its presence only in traces or because of its nanocrystalline coherent domains. The presence of both phases was confirmed by High-resolution STEM (see Fig. 5c & f). In addition, EDX linescans showing the quantitative determination of Mn and O atomic fraction and HRSTEM image simulations to confirm the crystal structures are reported in the Supporting Information, Figures S6 and S7, respectively.

In accordance with the CV reproduced in Fig. 1, the higher the step potential is the higher is the oxidation state of the final MnO_x deposit. Hence, it is not surprising that applying 0.6 V and 1.0 V resulted in the formation of manganese oxides with different stoichiometry. However, to the best of our knowledge, this simple but interesting finding has never been reported before. The difference between our studies with respect to the already reported investigations of the electrodeposition parameters effect on manganese oxides lies in the absence of dissolved O_2 in the Mn^{2+} electrolytic bath. This results in the formation of a mixture of δ-MnO_2 and MnOOH instead of pure δ-MnO_2 in correspondence with the oxidation peak centered at 0.8 V [16]. When the applied potential is even lower (0.6 V), the electro-oxidation of Mn^{2+} described in Section 3.1 is sluggish and only MnOOH is formed. Then, the thermally induced reduction and crystallization arise in the formation of Mn_3O_4 and Mn_2O_3 phases.

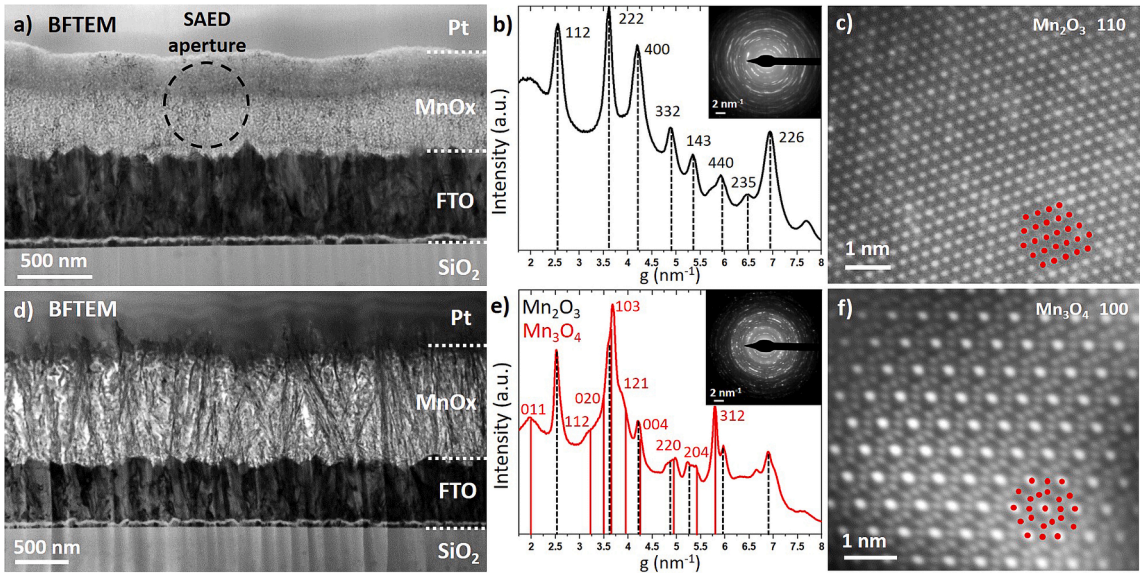

Fig. 5. Cross-sectional TEM investigation. a) Bright-field TEM image of the 1.0 V sample showing a dense network of MnO_x. b) Radially integrated SAED pattern (original in the inset) of the 1.0 V sample showing polycrystalline rings fitting to the cubic Mn_2O_3 phase. c) HRSTEM image of a Mn_2O_3 crystallite oriented along the 110 direction (Mn columns highlighted in red). d) BFTEM image of the 0.6 V sample with a fiber-like growth of MnO_x. e) Radially integrated SAED pattern (original in the inset) of the 0.6 V sample showing polycrystalline rings fitting to a mixture of Mn_2O_3 and Mn_3O_4. f) HRSTEM image of a selected Mn_3O_4 crystallite.

The information on the crystallite size and on internal strain of the electrodeposited MnO_x could be obtained from the full width at half maximum (FWHM) of the X-rays diffraction peaks. The FWHM (β) can be expressed as a linear combination of the contributions from the crystallite size (D) and the internal strain (ε) through the following Equation (3) [28]:

$$\frac{\beta cos\theta}{K\lambda} = \frac{1}{D} + \frac{\varepsilon sin\theta}{\lambda} \tag{3}$$

Where, λ is the X-ray wavelength (Cu-Kα = 1.5406 Å), θ the Bragg angle and K the shape constant. A plot of $\beta cos\theta/K\lambda$ versus $sin\theta/\lambda$, also known as Williamson-Hall (W-H) plot, gives a straight line whose y-axis intercept and slope provide information on the crystallite size and the internal strain generated within the crystal, respectively. If the internal stress ε is not taken in consideration, Eq. (3) converts to the Scherrer equation (Eq. (4)):

$$D = \frac{K\lambda}{\beta cos\theta} \tag{4}$$

In the following Table 1 the results of the average crystallite size directly measured from the TEM images (Fig. 5c and Supporting Information Figure S8) and obtained by applying Scherrer and Williamson-Hall equations to the XRD peaks are reported.

The values of crystallite size derived from the Scherrer equation are in good agreement with the observation of the TEM images for both the samples, while the W-H analysis resulted in higher values for the 1.0 V sample. An electron diffraction pattern taken from a small area of the 1.0 V sample in Fig. 6a reveals streak-like diffraction spots from a single coherent domain with a high angular spread. The (0 4 0) correspondent dark-field image (Fig. 6b) shows the spatial extent of a mosaic-like domain with a size in the range of a few hundred nanometers. The presence of the semi-coherent domains could explain the high value of internal stress in the 1.0 V sample as well as the larger crystallite size calculated from the W-H plot.

Table 1
Average crystallite size of 0.6 V and 1.0 V MnO_x calculated by using Scherrer equation, Williamson-Hall plot and directly measured from the TEM images.

Method	0.6 V crystallites size	1.0 V crystallites size
Scherrer	24 ± 4 nm	23 ± 3 nm
Williamson-Hall	32 ± 4 nm (internal strain = 0.1 %)	215 ± 3 nm (internal strain = 4.1 %)
TEM images	10 – 50 nm	20–25 nm ~ 300 nm semi-coherent domains

XPS analysis was performed to complement the XRD and TEM results and to investigate the effect of the thermal treatment on the MnO_x surface composition of the 0.6 V and 1.0 V samples. The valence state of Mn can be determined by the deconvolution of the Mn $2p_{3/2}$ peak as demonstrated by several authors [38–40] . However, this method has to deal with differential charging problems caused by the non-conductive nature of the sample. For this reason, we based the study of the Mn valence state on the deconvolution of the O 1 s spectrum and the measurement of the Mn 3 s doublet and $Mn2p_{3/2}$ – O 1 s peaks separation.

In Fig. 7 the O 1 s spectrum is deconvoluted into three components, related to different oxygen-containing bonds such as oxide (Mn–O–Mn bond) at 529.3–530.0 eV, hydroxide (Mn–O–H) at 530.5–531.5 eV and water (H–O–H) at 531.8–532.8 eV. Table 2 reports the quantitative analysis of the atomic percentage of each component: the thermally treated samples present a predominance of the Mn-O-Mn bonds on the surface, consistent with a reduction of the average oxidation state of MnO_x. The reduction of manganese oxide structure due to a thermal treatment in air has been reported in other studies [41,42].

The analysis of the Mn 3 s peaks multiplet splitting is useful to reveal a variation in the Mn valence state after the thermal treatment. In addition, it is possible to eliminate the errors of the calibration procedure by considering the peak separation instead of an absolute value of binding energy. The splitting of the Mn 3 s peaks is caused by the exchange interaction between 3 s and 3d electrons during the photoelectron ejection. The peak separation is related to the Mn valence state as following: the lower the valence is, the more electrons are present in the 3d orbital and the more interaction occurs upon photoelectron ejection. As a result, a lower valence state produces a wider splitting between the two components of the Mn 3 s multiplet. Data reported in Table 2 show that the Mn 3 s splitting increases from 5.3 to 5.4 eV and from 5.2 to 5.4 eV when the applied voltage is 0.6 V and 1.0 V respectively. Literature reports several estimations of the Mn valence based on the $\Delta E_{Mn\ 3s}$ value, including 4.5–4.8 eV for MnO_2, 5.2–5.4 eV for Mn_2O_3, 5.3 – 5.5 eV for Mn_3O_4 and 5.8 eV for MnO [43–46]. Unfortunately, the

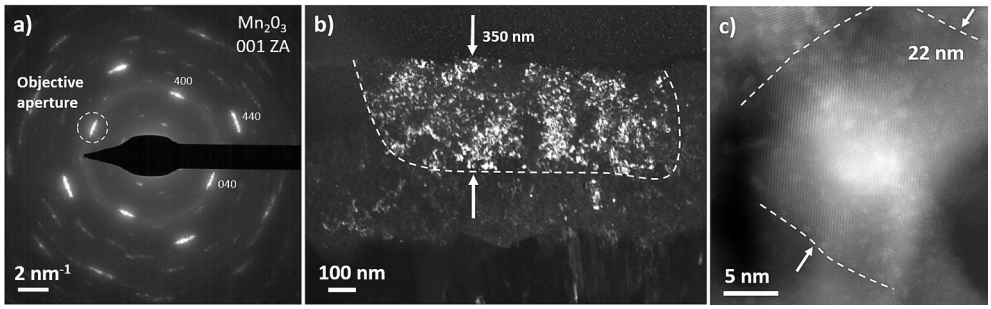

Fig. 6. Crystallite and domain size of the 1.0 V sample. a) SAED pattern of a crystallite in 001 orientation with a high angular spread. b) dark-field image based on a 040 type reflection showing a larger, mosaic-like domain of similar orientation. C) STEM image of a small crystal making contained in a mosaic domain.

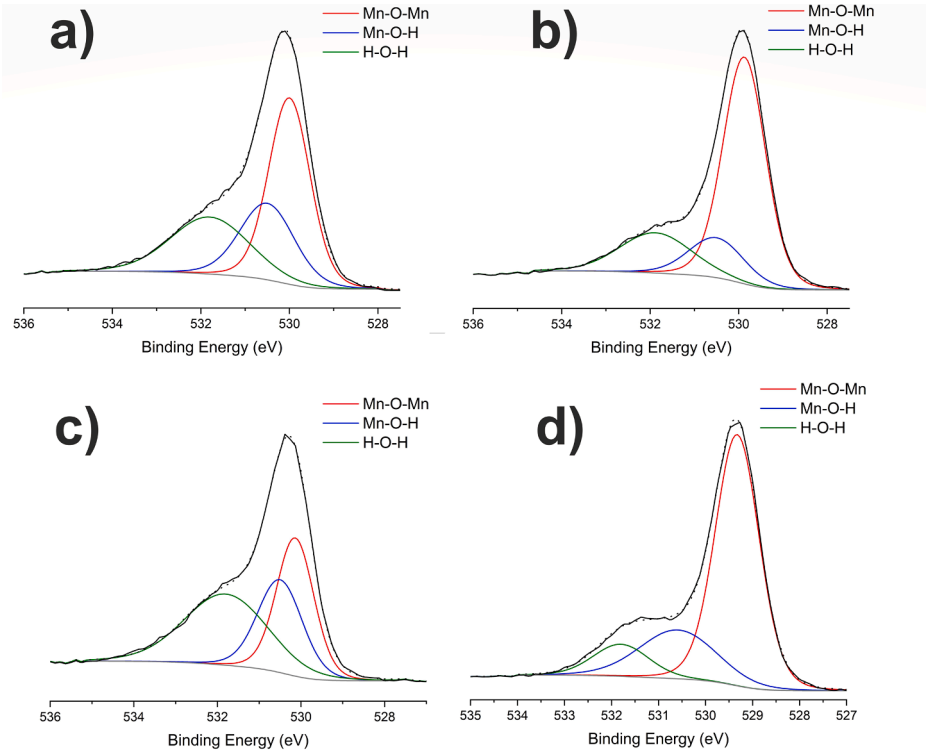

Fig. 7. XPS spectra of the O 1 s region. 0.6 V MnO_x a) as-electrodeposited, b) annealed; 1.0 V MnO_x c) as-electrodeposited, d) annealed.

Table 2
XPS peak analysis of O 1 s, Mn 3 s regions and $Mn2p_{3/2}$ – O 1 s energy separation of the MnO_x nanostructures.

	O 1 s Bond	Area %	Mn 3 s $\Delta E_{Mn\ 3s}$ (eV)	Mn $2p_{3/2}$ – O 1 s $\Delta E_{Mn\ 2p3/2\ -\ O\ 1s}$ (eV)
0.6 V	Mn-O-Mn	47.1	5.3	112.3
	Mn-O-H	25.6		
	H-O-H	27.3		
0.6 V annealed	Mn-O-Mn	65.4	5.4	112.1
	Mn-O-H	15.0		
	H-O-H	19.6		
1.0 V	Mn-O-Mn	33.9	5.2	112.6
	Mn-O-H	27.3		
	H-O-H	38.8		
1.0 V annealed	Mn-O-Mn	66.5	5.4	111.8
	Mn-O-H	22.9		
	H-O-H	10.6		

wide range of overlap between the results reported in the literature prevents an accurate estimation of the valence state of Mn from the $\Delta E_{Mn\ 3s}$ values obtained in our analysis. To further support the reduction of the MnO_x surface composition after the thermal treatment, we reported in Table 2 the values of the binding energy separation between the Mn $2p_{3/2}$ and the Mn-O-Mn peaks. A decrease in the $\Delta E_{Mn\ 2p3/2\ -\ O\ 1s}$ is correlated with a reduced valence, in accordance with the work of previous authors [43,44]. The Mn 2p spectra and the deconvolution of the Mn 3 s region are reported in the Supporting Information, Figure S9 and S10, respectively.

3.5. Optical properties

The performance of a functional material in the photoelectrochemistry field is mainly determined by its optical properties such as optical absorption, energy band gap and electron-hole pairs recombination. Fig. 8 represents the UV–vis absorption spectra of the sample synthetized at 0.6 V and 1.0 V before and after the thermal treatment.

The as-electrodeposited MnO_x possess an absorption peak at around 380 nm, which is tailed to the visible region. Sakai *et al.* [47] reported the same value for their MnO_2 structures with nanosheets-like morphology. It is interesting to notice the thermal treatment has only

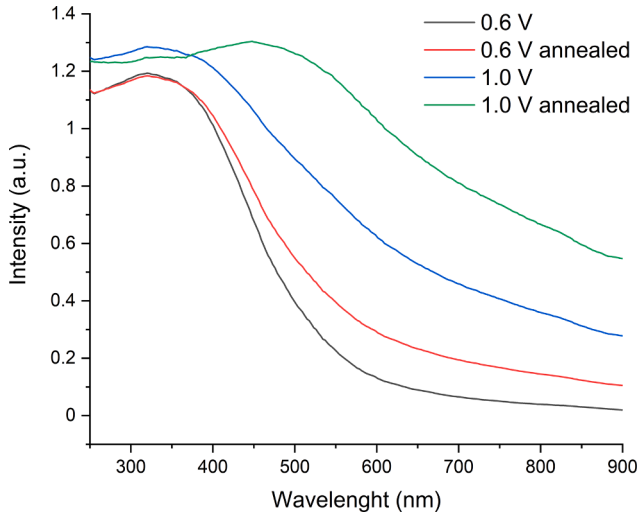

Fig. 8. UV–vis absorption spectra. 0.6 V MnO_x (black line as-electrodeposited, red line annealed) and 1.0 V MnO_x (blue line as-electrodeposited, green line annealed).

a slight effect on the optical absorption of the MnO_x synthetized at 0.6 V, resulting in a small increase of the absorption in the wavelength range 400 – 900 nm. On the other hand, the thermal treatment causes a notable red-shift, in addition to an increase in the absorption intensity for the 1.0 V MnO_x. Using the UV–vis absorption spectra, other optical constants including the complex refractive index and the complex dielectric function have been estimated and reported in the Supporting Information (Figure S11 and S12, respectively) [48]. However, only a few studies on manganese oxides are reporting the variation of the complex refractive index and dielectric function with the wavelength of the radiation [49]. Given also the intrinsic limitation of the technique, it is difficult to provide a proper comparison based on these parameters.

The band gap of the MnO_x deposits is calculated from the UV–vis absorption spectra by using the Tauc's equation (Eq. (5)):

$$(\alpha h\nu)^{1/n} = A(h\nu - E_g) \quad (5)$$

Where α is the absorption coefficient, h is the Planck's constant, ν is the photon frequency, A is a proportional constant and E_g is the band gap. The exponent n denotes the nature of the electronic transition and it assumes the value of $n = \frac{1}{2}$ and $n = 2$ for direct and indirect allowed transitions respectively. The Tauc plots for the direct transitions are reported in Fig. 9.

The extrapolated values of the band gap are in agreement with the UV–vis results, remarking a general decrease of the energy gap for the annealed samples. As for the UV–vis absorption peak, the red shift is more significant for the 1.0 V MnO_x, which is subjected to a E_g reduction from 2.3 eV to 1.8 eV. If we consider that the visible domain extends in the energy interval 1.8 – 3.2 eV (which correspond to the wavelength range 700–380 nm), a red-shift in the band gap is beneficial for the optical absorption properties of the MnO_x nanostructures. A smaller band gap allows the MnO_x to absorb in a wider range of wavelengths, thus increasing the absorption intensity in the visible light region, as shown in Fig. 9. The values of band gap obtained in our study are in good agreement with those reported in Table 3 and in the literature [50–53]. The indirect Tauc plots are reported Fig. 10.

The absence of a horizontal baseline makes the extrapolation of a

Table 3
Comparison between band gap, conduction and valence band edges values.

Authors	Sample	Method	$E_g(eV)$	$E_{VB}(eV)$	$E_{CB}(eV)$
This work	0.6 V	UV–vis	2.6	2.67	0.07
	0.6 V annealed	absorption	2.5	2.20	−0.3
	1.0 V		2.3	2.52	0.22
	1.0 V annealed		1.8	1.97	0.17
Sakai *et al.* [47]	MnO_2	Photocurrent onset	2.23	1.85	−0.35
Salari *et al.* [58]	MnO_2	UV–vis absorption	1.77	2.34	0.57
Blaise *et al.* [54]	Na-MnO_2	Open circuit potential	2.1	2.78	0.68
		Photocurrent onset		3.34	1.24
		Mott-Schottky		3.43	1.33

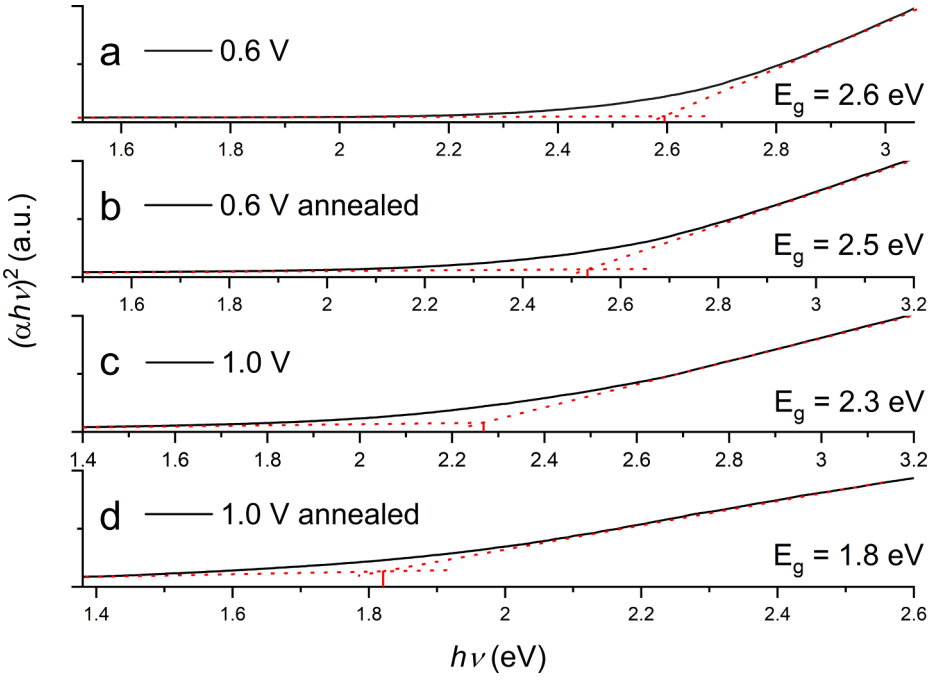

Fig. 9. Direct Tauc plots. 0.6 V MnO_x a) as-electrodeposited, b) annealed; 1.0 V MnO_x c) as-electrodeposited, d) annealed.

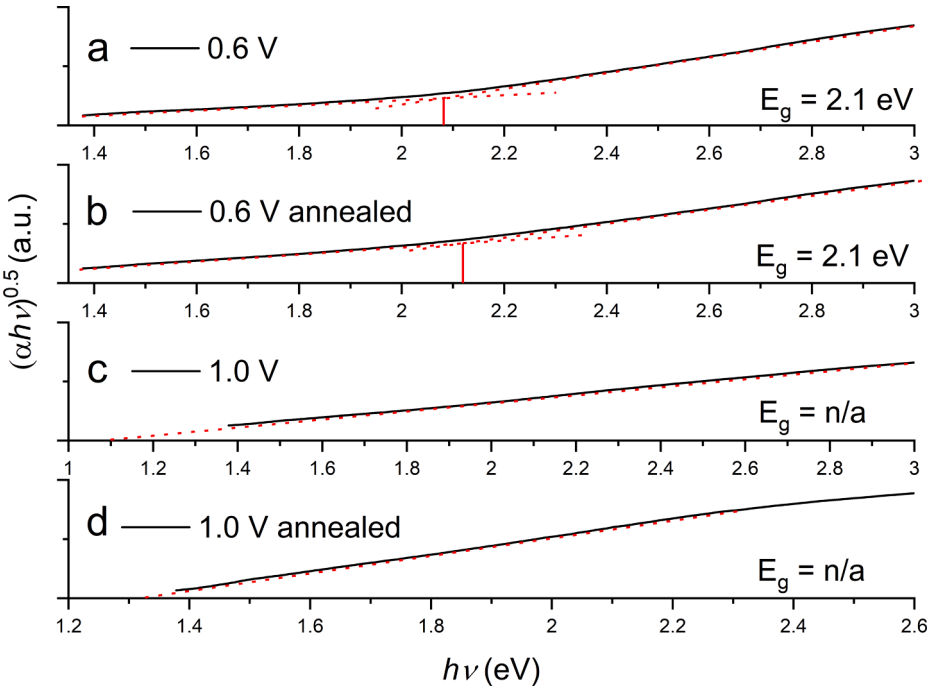

Fig. 10. Indirect Tauc plots. 0.6 V MnO_x a) as-electrodeposited, b) annealed; 1.0 V MnO_x c) as-electrodeposited, d) annealed.

reliable band gap value for the MnO_x synthesized at 1.0 V difficult. For this reason, we preferred to indicate the E_g value as not applicable (n/a). The 0.6 V MnO_x have almost the same band gap value (2.1 eV). A lower value for the indirect rather than direct band gap has been reported in the literature for manganese oxide-based structures [51,53,54].

The band edge position of the valence band, E_{VB}, and the conduction band, E_{CB}, is determined by the following Eq. (6) and Eq. (7) [55]:

$$E_{VB} = X - E^e + \frac{1}{2}E_g \tag{6}$$

$$E_{CB} = E_{VB} - E_g \tag{7}$$

Where E^e is the energy of free electrons on the hydrogen scale ($E^e = 4.44eV$ [56]) and X the electronegativity of the semiconductor calculated as the geometric mean of the electronegativity of the constituent atoms, according to the work of Mulliken [57]. Table 3 reports the band edge positions calculated within this study including a comparison with data from the literature.

There is good agreement between our results and the literature despite the values of the band edges being affected by many factors such as: (i) the limitations of the methods used for the estimation [54], (ii) the chemical and microstructural properties of the samples.

Photoluminescence measurements provide useful information about the electron-hole recombination in the semiconducting MnO_x nanostructures. A low intensity of the photoluminescence peak indicates a low recombination and thus better optical properties. Fig. 11 shows the PL spectra of the MnO_x synthetized at 0.6 V and 1.0 V before and after the thermal treatment.

The PL intensity of the annealed MnO_x nanostructures is lower than that of the as-electrodeposited MnO_x. The reduction of the PL intensity is calculated to be around 30 % and 40 % of the initial value for the 0.6 V and 1.0 V MnO_x respectively.

Therefore, the thermal treatment is highly beneficial in enhancing the charge separation of the photo-induced electron-hole pairs. The dependence of the yield of photogenerated charges on the crystallinity of several inorganic materials has been studied in previous works [47–49].

A well-ordered crystalline structure usually enables a more efficient

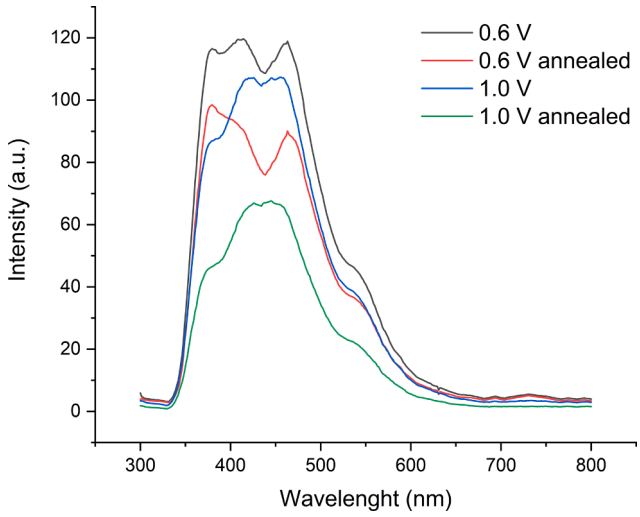

Fig. 11. Photoluminescence spectra. 0.6 V MnO_x (black line as-electrodeposited, red line annealed); 1.0 V MnO_x (blue line as-electrodeposited, green line annealed).

charge separation and an increase in the lifetime of the photogenerated charges. Besides, thermally created defects, such as oxygen vacancies, could behave as active centers for the adsorption of molecular oxygen [59–61]. Molecular oxygen is an electron scavenger, thus, the photogenerated holes experience prolonged lifetimes thanks to a reduction in the recombination rate with electrons.

Finally and yet important to mention, a significant contribution to the enhancement of the optical properties is given by the manganese oxide phase. We described how the 1.0 V annealed sample, which present the Mn_2O_3 stoichiometry, possesses a much favorable absorption of visible light as well as reduced electron-hole pairs recombination with respect to the 0.6 V sample (mainly composed of Mn_3O_4). The reason of those differences could be due several factors including: (i) the larger crystallite size and (ii) the more compact and less porous microstructure of Mn_2O_3 compared with Mn_3O_4 (see TEM cross section images, Fig. 5a

& 5d).

4. Conclusion

In this work we successfully synthesized two different phases of manganese oxide, Mn_3O_4 and Mn_2O_3, with a new electrodeposition route based on the removal of the dissolved O_2 from the electrolytic bath. A systematic investigation of the effect of the electrodeposition parameters allowed us to optimize the synthesis conditions to have the best control over the final surface morphology, microstructure and stoichiometry of the deposited MnO_x. Discrete clusters, petal-shaped interconnected nanosheets and nanoflake-like morphologies are obtained by simply favoring/preventing the mass diffusion of Mn^{2+} ions at the electrode during the electrodeposition process. We clarify the role of the applied potential on the average manganese oxidation state obtaining Mn_3O_4 or Mn_2O_3 when 0.6 V or 1.0 V are respectively applied. TEM cross section images revealed two distinct microstructures: fiber-like growth with open porosity for Mn_3O_4, more compact and less porous microstructure for Mn_2O_3. The analysis of the UV–vis and photoluminescence spectra suggests that the thermally treated manganese oxides possess enhanced optical absorption and charge separation properties. The development of a crystalline structure together with crystallite size and microstructure of the different phases are considered the main factors affecting the optical properties. Overall, the results herein reported emphasize the importance of the control over stoichiometry, crystallinity and microstructure of electrodeposited MnO_x for the enhancement of the optical properties. This is of extraordinary importance for the future applications of manganese oxides in the field of catalysis, photovoltaics and water splitting.

CRediT authorship contribution statement

Roberto Cestaro: Conceptualization, Methodology, Validation, Investigation, Writing – original draft, Writing – review & editing. **Peter Schweizer:** Conceptualization, Investigation. **Laetitia Philippe:** Conceptualization, Supervision. **Xavier Maeder:** Supervision. **Albert Serrà:** Conceptualization, Methodology, Supervision.

Declaration of Competing Interest

The authors declare that they have no known competing financial interests or personal relationships that could have appeared to influence the work reported in this paper.

Acknowledgements

The authors would like to acknowledge Metrohm foundation for the financial support of this research.

Appendix A. Supplementary data

Supplementary data to this article can be found online at https://doi.org/10.1016/j.apsusc.2021.152289.

References

[1] H. Veeramani, D. Aruguete, N. Monsegue, M. Murayama, U. Dippon, A. Kappler, M. F. Hochella, Low-Temperature Green Synthesis of Multivalent Manganese Oxide Nanowires, ACS Sustain. Chem. Eng. 1 (9) (2013) 1070–1074, https://doi.org/10.1021/sc400129n.

[2] V. Kumar, K. Singh, S. Panwar, S.K. Mehta, Green synthesis of manganese oxide nanoparticles for the electrochemical sensing of p-nitrophenol, Int. Nano Lett. 7 (2) (2017) 123–131, https://doi.org/10.1007/s40089-017-0205-3.

[3] H. Zhang, A. Wu, H. Fu, L. Zhang, H. Liu, S. Zheng, H. Wan, Z. Xu, Efficient removal of Pb(II) ions using manganese oxides: the role of crystal structure, RSC Adv. 7 (2017) 41228–41240, https://doi.org/10.1039/C7RA05955H.

[4] M. Augustin, D. Fenske, I. Bardenhagen, A. Westphal, M. Knipper, T. Plaggenborg, J. Kolny-Olesiak, J. Parisi, Manganese oxide phases and morphologies: A study on calcination temperature and atmospheric dependence, Beilstein J. Nanotechnol. 6 (2015) 47–59, https://doi.org/10.3762/bjnano.6.6.

[5] S.-C. Pang, M.A. Anderson, T.W. Chapman, Novel Electrode Materials for Thin-Film Ultracapacitors: Comparison of Electrochemical Properties of Sol-Gel-Derived and Electrodeposited Manganese Dioxide, J. Electrochem. Soc. 147 (2) (2000) 444, https://doi.org/10.1149/1.1393216.

[6] M. Toupin, T. Brousse, D. Bélanger, Influence of microstucture on the charge storage properties of chemically synthesized manganese dioxide, Chem. Mater. 14 (9) (2002) 3946–3952, https://doi.org/10.1021/cm020408q.

[7] S.W. Lee, J. Kim, S. Chen, P.T. Hammond, Y. Shao-Horn, Carbon Nanotube/Manganese Oxide Ultrathin Film Electrodes for Electrochemical Capacitors, ACS Nano 4 (7) (2010) 3889–3896, https://doi.org/10.1021/nn100681d.

[8] C.-C. Hu, Y.-T. Wu, K.-H. Chang, Low-temperature hydrothermal synthesis of Mn3O4 and MnOOH single crystals: Determinant influence of oxidants, Chem. Mater. 20 (9) (2008) 2890–2894, https://doi.org/10.1021/cm703245k.

[9] K.R. Prasad, N. Miura, Potentiodynamically deposited nanostructured manganese dioxide as electrode material for electrochemical redox supercapacitors, J. Power Sources. 135 (1-2) (2004) 354–360, https://doi.org/10.1016/j.jpowsour.2004.04.005.

[10] W. Huang, J. Li, Y. Xu, Nucleation/growth mechanisms and morphological evolution of porous MnO2 coating deposited on graphite for supercapacitor, Materials (Basel). 10 (2017) 1205, https://doi.org/10.3390/ma10101205.

[11] M. Huynh, D.K. Bediako, Y.i. Liu, D.G. Nocera, Nucleation and growth mechanisms of an electrodeposited manganese oxide oxygen evolution catalyst, J. Phys. Chem. C. 118 (30) (2014) 17142–17152, https://doi.org/10.1021/jp501768n.

[12] A. Ramírez, P. Hillebrand, D. Stellmach, M.M. May, P. Bogdanoff, S. Fiechter, Evaluation of MnOx, Mn2O3, and Mn 3O4 electrodeposited films for the oxygen evolution reaction of water, J. Phys. Chem. C. 118 (26) (2014) 14073–14081, https://doi.org/10.1021/jp500939d.

[13] W. Chen, N. Wang, L.i. Liu, Y. Cui, X. Cao, Q. Chen, L. Guo, Facile synthesis of manganite nanowires: Phase transitions and their electrocatalysis performance, Nanotechnology. 20 (44) (2009) 445601, https://doi.org/10.1088/0957-4484/20/44/445601.

[14] B. Deljoo, H. Tan, S.L. Suib, M. Aindow, Thermally activated structural transformations in manganese oxide nanoparticles under air and argon atmospheres, J. Mater. Sci. 55 (17) (2020) 7247–7258, https://doi.org/10.1007/s10853-020-04525-6.

[15] C.J. Clarke, G.J. Browning, S.W. Donne, An RDE and RRDE study into the electrodeposition of manganese dioxide, Electrochim. Acta. 51 (26) (2006) 5773–5784, https://doi.org/10.1016/j.electacta.2006.03.013.

[16] N. Larabi-Gruet, S. Peulon, A. Lacroix, A. Chaussé, Studies of electrodeposition from Mn(II) species of thin layers of birnessite onto transparent semiconductor, Electrochim. Acta. 53 (24) (2008) 7281–7287, https://doi.org/10.1016/j.electacta.2008.03.080.

[17] M. Ndjeri, S. Peulon, M.L. Schlegel, A. Chaussé, In situ grazing-incidence X-ray diffraction during electrodeposition of birnessite thin films: Identification of solid precursors, Electrochem. Commun. 13 (5) (2011) 491–494, https://doi.org/10.1016/j.elecom.2011.02.029.

[18] M. Nakayama, A. Tanaka, Y. Sato, T. Tonosaki, K. Ogura, Electrodeposition of manganese and molybdenum mixed oxide thin films and their charge storage properties, Langmuir 21 (13) (2005) 5907–5913, https://doi.org/10.1021/la050114u10.1021/la050114u.s001.

[19] Z. Rogulski, H. Siwek, I. Paleska, A. Czerwiński, Electrochemical behavior of manganese dioxide on a gold electrode, J. Electroanal. Chem. 543 (2) (2003) 175–185, https://doi.org/10.1016/S0022-0728(03)00045-7.

[20] M. Fleischmann, H.R. Thirsk, I.M. Tordesillas, Kinetics of electrodeposition of γ-manganese dioxide, Trans. Faraday Soc. 58 (1962) 1865–1877, https://doi.org/10.1039/tf9625801865.

[21] B. Babakhani, D.G. Ivey, Effect of electrodeposition conditions on the electrochemical capacitive behavior of synthesized manganese oxide electrodes, J. Power Sources. 196 (24) (2011) 10762–10774, https://doi.org/10.1016/j.jpowsour.2011.08.102.

[22] B. Babakhani, D.G. Ivey, Anodic deposition of manganese oxide electrodes with rod-like structures for application as electrochemical capacitors, J. Power Sources. 195 (7) (2010) 2110–2117, https://doi.org/10.1016/j.jpowsour.2009.10.045.

[23] W. Wei, X. Cui, X. Mao, W. Chen, D.G. Ivey, Morphology evolution in anodically electrodeposited manganese oxide nanostructures for electrochemical supercapacitor applications - Effect of supersaturation ratio, Electrochim. Acta. 56 (3) (2011) 1619–1628, https://doi.org/10.1016/j.electacta.2010.10.044.

[24] A. Mathur, R. Kaushik, A. Halder, Visible-light-driven photo-enhanced zinc-air batteries using synergistic effect of different types of MnO2nanostructures, Catal. Sci. Technol. 10 (21) (2020) 7352–7364.

[25] P.F. Smith, B.J. Deibert, S. Kaushik, G. Gardner, S. Hwang, H. Wang, J.F. Al-Sharab, E. Garfunkel, L. Fabris, J. Li, G.C. Dismukes, Coordination Geometry and Oxidation State Requirements of Corner-Sharing MnO6 Octahedra for Water Oxidation Catalysis: An Investigation of Manganite (γ-MnOOH), ACS Catal. 6 (3) (2016) 2089–2099, https://doi.org/10.1021/acscatal.6b0009910.1021/acscatal.6b00099.s001.

[26] X. Ye, X. Jiang, L. Chen, W. Jiang, H. Wang, W. Cen, S. Ma, Effect of manganese dioxide crystal structure on adsorption of SO2 by DFT and experimental study, Appl. Surf. Sci. 521 (2020) 146477, https://doi.org/10.1016/j.apsusc.2020.146477.

[27] W. Yang, Z. Su, Z. Xu, W. Yang, Y. Peng, J. Li, Comparative study of α-, β-, γ- and δ-MnO2 on toluene oxidation: Oxygen vacancies and reaction intermediates, Appl. Catal. B Environ. 260 (2020) 118150, https://doi.org/10.1016/j.apcatb.2019.118150.

[28] Y. Liu, J. Wei, Y. Tian, S. Yan, The structure-property relationship of manganese oxides: Highly efficient removal of methyl orange from aqueous solution, J. Mater. Chem. A. 3 (37) (2015) 19000–19010.
[29] J. Zhang, Y. Li, L. Wang, C. Zhang, H. He, Catalytic oxidation of formaldehyde over manganese oxides with different crystal structures, Catal, Sci. Technol. 5 (4) (2015) 2305–2313, https://doi.org/10.1039/C4CY01461H.
[30] D.M. Robinson, Y.B. Go, M. Mui, G. Gardner, Z. Zhang, D. Mastrogiovanni, E. Garfunkel, J. Li, M. Greenblatt, G.C. Dismukes, Photochemical water oxidation by crystalline polymorphs of manganese oxides: Structural requirements for catalysis, J. Am. Chem. Soc. 135 (9) (2013) 3494–3501, https://doi.org/10.1021/ja310286h.
[31] Y.-S. Chen, C.-C. Hu, Y.-T. Wu, Capacitive and textural characteristics of manganese oxide prepared by anodic deposition: Effects of manganese precursors and oxide thickness, J. Solid State Electrochem. 8 (7) (2004) 467–473, https://doi.org/10.1007/s10008-004-0500-6.
[32] S. Rodrigues, N. Munichandraiah, A.K. Shukla, A cyclic voltammetric study of the kinetics and mechanism of electrodeposition of manganese dioxide, J. Appl. Electrochem. 28 (1998) 1235–1241, https://doi.org/10.1023/A:1003472901760.
[33] A.D. Cross, A. Morel, T.F. Hollenkamp, S.W. Donne, Chronoamperometric Versus Galvanostatic Preparation of Manganese Oxides for Electrochemical Capacitors, J. Electrochem. Soc. 158 (10) (2011) A1160, https://doi.org/10.1149/1.3625581.
[34] S. Nijjer, J. Thonstad, G.M. Haarberg, Oxidation of manganese(II) and reduction of manganese dioxide in sulphuric acid, Electrochim. Acta. 46 (2-3) (2000) 395–399, https://doi.org/10.1016/S0013-4686(00)00597-1.
[35] M.-T. Lee, J.-K. Chang, Y.-T. Hsieh, W.-T. Tsai, C.-K. Lin, Manganese oxide thin films prepared by potentiodynamic electrodeposition and their supercapacitor performance, J. Solid State Electrochem. 14 (9) (2010) 1697–1703, https://doi.org/10.1007/s10008-010-1009-9.
[36] C.-C. Hu, C.-C. Wang, Nanostructures and Capacitive Characteristics of Hydrous Manganese Oxide Prepared by Electrochemical Deposition, J. Electrochem. Soc. 150 (8) (2003) A1079, https://doi.org/10.1149/1.1587725.
[37] N. Sergienko, J. Radjenovic, Manganese oxide-based porous electrodes for rapid and selective (electro)catalytic removal and recovery of sulfide from wastewater, Appl. Catal. B Environ. 267 (2020) 118608, https://doi.org/10.1016/j.apcatb.2020.118608.
[38] M. Oku, K. Hirokawa, S. Ikeda, X-ray photoelectron spectroscopy of manganese—oxygen systems, J. Electron Spectros. Relat. Phenomena. 7 (5) (1975) 465–473, https://doi.org/10.1016/0368-2048(75)85010-9.
[39] H.W. Nesbitt, D. Banerjee, Interpretation of XPS Mn(2p) spectra of Mn oxyhydroxides and constraints on the mechanism of MnO 2 precipitation, Am. Mineral. 83 (3-4) (1998) 305–315, https://doi.org/10.2138/am-1998-3-414.
[40] M.C. Biesinger, B.P. Payne, A.P. Grosvenor, L.W.M. Lau, A.R. Gerson, R.S.C. Smart, Resolving surface chemical states in XPS analysis of first row transition metals, oxides and hydroxides: Cr, Mn, Fe, Co and Ni, Appl. Surf. Sci. 257 (7) (2011) 2717–2730, https://doi.org/10.1016/j.apsusc.2010.10.051.
[41] S.H. Kim, S.J. Kim, S.M. Oh, Preparation of layered MnO2 via thermal decomposition of KMnO4 and its electrochemical characterizations, Chem. Mater. 11 (3) (1999) 557–563, https://doi.org/10.1021/cm9801643.
[42] T.E. Moore, M. Ellis, P.W. Selwood, Solid Oxides and Hydroxides of Manganese 1, J. Am. Chem. Soc. 72 (2) (1950) 856–866, https://doi.org/10.1021/ja01158a056.
[43] M. Chigane, M. Ishikawa, Manganese Oxide Thin Film Preparation by Potentiostatic Electrolyses and Electrochromism, J. Electrochem. Soc. 147 (6) (2000) 2246, https://doi.org/10.1149/1.1393515.
[44] M. Toupin, T. Brousse, D. Bélanger, Charge storage mechanism of MnO2 electrode used in aqueous electrochemical capacitor, Chem. Mater. 16 (16) (2004) 3184–3190, https://doi.org/10.1021/cm049649j10.1021/cm049649j.s001.
[45] E.S. Ilton, J.E. Post, P.J. Heaney, F.T. Ling, S.N. Kerisit, XPS determination of Mn oxidation states in Mn (hydr)oxides, Appl. Surf. Sci. 366 (2016) 475–485, https://doi.org/10.1016/j.apsusc.2015.12.159.
[46] B. Djurfors, J.N. Broughton, M.J. Brett, D.G. Ivey, Electrochemical oxidation of Mn/MnO films: Formation of an electrochemical capacitor, Acta Mater. 53 (4) (2005) 957–965, https://doi.org/10.1016/j.actamat.2004.10.041.
[47] N. Sakai, Y. Ebina, K. Takada, T. Sasaki, Photocurrent generation from semiconducting manganese oxide nanosheets in response to visible light, J. Phys. Chem. B. 109 (19) (2005) 9651–9655, https://doi.org/10.1021/jp0500485.
[48] J. Singh, Optical Properties of Condensed Matter and Applications - Wiley Series in Materials for Electronic - amp -, Optoelectronic Applications (2006).
[49] H. Jamil, M. Khaleeq-ur-Rahman, I.M. Dildar, S. Shaukat, Structural and optical properties of manganese oxide thin films deposited by pulsed laser deposition at different substrate temperatures, Laser Phys. 27 (9) (2017) 096101, https://doi.org/10.1088/1555-6611/aa7cc8.
[50] B.D. Viezbicke, S. Patel, B.E. Davis, D.P. Birnie, Evaluation of the Tauc method for optical absorption edge determination: ZnO thin films as a model system, Phys. Status Solidi Basic Res. 252 (8) (2015) 1700–1710.
[51] S. Liu, H. Liu, G. Jin, H. Yuan, Preparation of a novel flower-like MnO2/BiOI composite with highly enhanced adsorption and photocatalytic activity, RSC Adv. 5 (57) (2015) 45646–45653.
[52] K.P. Ganesan, N. Anandhan, G. Gopu, A. Amaliroselin, T. Marimuthu, R. Paneerselvam, An enhancement of ferromagnetic, structural, morphological, and optical properties of Mn-doped Cu2O thin films by an electrodeposition technique, J. Mater. Sci. Mater. Electron. 30 (21) (2019) 19524–19535, https://doi.org/10.1007/s10854-019-02318-5.
[53] K. Saravanakumar, V. Muthuraj, S. Vadivel, Constructing novel Ag nanoparticles anchored on MnO2 nanowires as an efficient visible light driven photocatalyst, RSC Adv. 6 (66) (2016) 61357–61366.
[54] B.A. Pinaud, Z. Chen, D.N. Abram, T.F. Jaramillo, Thin films of sodium birnessite-type MnO2: Optical properties, electronic band structure, and solar photoelectrochemistry, J. Phys. Chem. C. 115 (23) (2011) 11830–11838, https://doi.org/10.1021/jp200015p.
[55] A.H. Nethercot, Prediction of Fermi energies and photoelectric thresholds based on electronegativity concepts, Phys. Rev. Lett. 33 (18) (1974) 1088–1091, https://doi.org/10.1103/PhysRevLett.33.1088.
[56] S. Trasatti, The absolute electrode potential: an explanatory note (Recommendations 1986), Pure Appl. Chem. 58 (1986) (1986) 955–966, https://doi.org/10.1351/pac198658070955.
[57] Robert S. Mulliken, A new electroaffinity scale; Together with data on valence states and on valence ionization potentials and electron affinities, J. Chem. Phys. 2 (11) (1934) 782–793, https://doi.org/10.1063/1.1749394.
[58] Hadi Salari, Hajar Hasan Hosseini, In situ synthesis of visible-light-driven a-MnO2 nanorod/AgBr nanocomposites for increased photoinduced charge separation and enhanced photocatalytic activity, Mater. Res. Bull. 133 (2021) 111046, https://doi.org/10.1016/j.materresbull.2020.111046.
[59] Jing Liqiang, Qu Yichun, Wang Baiqi, Li Shudan, Jiang Baojiang, Yang Libin, Fu Wei, Fu Honggang, Sun Jiazhong, Review of photoluminescence performance of nano-sized semiconductor materials and its relationships with photocatalytic activity, Sol. Energy Mater. Sol. Cells. 90 (12) (2006) 1773–1787, https://doi.org/10.1016/j.solmat.2005.11.007.
[60] N. Bansal, L.X. Reynolds, A. MacLachlan, T. Lutz, R.S. Ashraf, W. Zhang, C. B. Nielsen, I. McCulloch, D.G. Rebois, T. Kirchartz, M.S. Hill, K.C. Molloy, J. Nelson, S.A. Haque, Influence of crystallinity and energetics on charge separation in polymer-inorganic nanocomposite films for solar cells, Sci. Rep. 3 (2013) 1–8, https://doi.org/10.1038/srep01531.
[61] Tracy L. Thompson, John T. Yates, TiO2-based Photocatalysis: Surface Defects, Oxygen and Charge Transfer, Top. Catal. 35 (3-4) (2005) 197–210, https://doi.org/10.1007/s11244-005-3825-1.